

Do All Candle-Flame-Shaped Flares Have the Same Temperature Distribution?

Tingyu Gou^{1,2} · Rui Liu¹ · Yuming Wang^{1,3}

Received: 7 April 2015 / Accepted: 23 July 2015 / Published online: 11 August 2015
© Springer Science+Business Media Dordrecht 2015

Abstract We performed a differential emission measure (DEM) analysis of candle-flame-shaped flares observed with the *Atmospheric Imaging Assembly* onboard the *Solar Dynamic Observatory*. The DEM profile of flaring plasmas generally exhibits a double peak distribution in temperature, with a cold component around $\log T \approx 6.2$ and a hot component around $\log T \approx 7.0$. Attributing the cold component mainly to the coronal background, we propose a mean temperature weighted by the hot DEM component as a better representation of flaring plasma than the conventionally defined mean temperature, which is weighted by the whole DEM profile. Based on this corrected mean temperature, the majority of the flares studied, including a confined flare with a double candle-flame shape sharing the same cusp-shaped structure, resemble the famous Tsuneta flare in temperature distribution, *i.e.*, the cusp-shaped structure has systematically higher temperatures than the rounded flare arcade underneath. However, the M7.7 flare on 19 July 2012 poses a very intriguing violation of this paradigm: the temperature decreases with altitude from the tip of the cusp toward the top of the arcade; the hottest region is slightly above the X-ray loop-top source that is

R. Liu is a member of Collaborative Innovation Center of Astronautical Science and Technology, China.

Electronic supplementary material The online version of this article (doi:[10.1007/s11207-015-0750-8](https://doi.org/10.1007/s11207-015-0750-8)) contains supplementary material, which is available to authorized users.

✉ R. Liu
rliu@ustc.edu.cn

T. Gou
tygou@mail.ustc.edu.cn

Y. Wang
ymwang@ustc.edu.cn

- ¹ CAS Key Laboratory of Geospace Environment, Department of Geophysics and Planetary Sciences, University of Science and Technology of China, Hefei, Anhui 230026, China
- ² Mengcheng National Geophysical Observatory, School of Earth and Space Sciences, University of Science and Technology of China, Hefei, Anhui 230026, China
- ³ Synergetic Innovation Center of Quantum Information and Quantum Physics, University of Science and Technology of China, Hefei, Anhui 230026, China

co-spatial with the emission-measure-enhanced region at the top of the arcade. This signifies that a different heating mechanism from the slow-mode shocks attached to the reconnection site operates in the cusp region during the flare decay phase.

Keywords Flares, dynamics · Heating, in flares

1. Introduction

The sudden, explosive release of magnetic free energy in the solar atmosphere often manifests as three closely related phenomena, namely, flares, prominence/filament eruptions, and coronal mass ejections (CMEs). As one of the most important discoveries of the *Yohkoh* mission (Ogawara *et al.*, 1991) that helped shape the modern vision of solar flares, candle-flame-shaped flares (Tsuneta *et al.*, 1992) serve as important evidence for magnetic reconnection and have received much attention (*e.g.*, Tsuneta, 1996; Forbes and Acton, 1996; Reeves, Seaton, and Forbes, 2008; Guidoni *et al.*, 2015). In one such flare (21 February 1992, also known as the “Tsuneta flare”), it was found that the outer flare loops have systematically higher temperatures in excess of 10 MK, forming a sharp, cusp-shaped structure above the cooler, round-shaped flare arcade (Tsuneta, 1996). Within the framework of the classical CSHKP model (Carmichael, 1964; Sturrock, 1966; Hirayama, 1974; Kopp and Pneuman, 1976), the cusp-shaped structure is identified with newly reconnected field lines, which subsequently retract away from the reconnection site driven by magnetic tension force and eventually relax into the rounded field lines piling up on top of the flare arcade. This growth of the flare arcade, associated with separating flare ribbons serving as its footprints in the chromosphere, is explained by the reconnection at progressively higher altitudes in the corona, with newly reconnected hot loops mapping to the tip of the cusp.

Models also predict the development of slow-mode shocks in the vicinity of the reconnection site (Priest and Forbes, 1986, and references therein), which annihilate the magnetic field in the plasma flowing through the shocks. The liberated thermal energy is conducted along the newly reconnected field lines, heating the low-density plasma ‘frozen’ into the field. As the conduction fronts reach the chromosphere, chromospheric plasmas evaporate and fill up the reconnected flux tubes with high-density material emitting soft X-rays (Antiochos and Sturrock, 1978; Schmieder *et al.*, 1987). Meanwhile, the accelerated particles precipitate along the field lines and are thermalized in the chromosphere, emitting hard X-rays. This process also contributes significantly to chromospheric evaporation, especially in the impulsive phase, but may play a less important role in the decay phase (Fletcher *et al.*, 2011).

Candle-flame-shaped flares are normally long-duration events (LDE: Sheeley *et al.*, 1983; Webb and Hundhausen, 1987) with a gradual decay phase lasting for hours as opposed to confined flares (Shibata and Magara, 2011). However, Liu *et al.* (2014) presented the observation of an X-class LDE that exhibited a cusp-shaped structure above an arcade of flare loops but was clearly confined. Moreover, the cusp-shaped structure consisted of multiple nested loops that repeatedly rose upward and disappeared when approaching the cusp edge; the temperature was highest at the top of the arcade and became cooler toward the tip of the cusp. These features contradict the standard picture of flares. Liu *et al.* (2014) further demonstrated that instead of X- or Y-type neutral lines that are often attributed to candle-flame-shaped flares (Priest and Forbes, 2002) the quasi-separatrix layers

(Titov, Hornig, and Démoulin, 2002) involved in a tripolar magnetic configuration are responsible for this atypical cusp-shaped structure. A further question hence arises as regards whether all candle-flame-shaped flares have the same temperature distribution as the Tsuneta flare.

In this article, we investigate the candle-flame-shaped flares observed in EUV by the *Atmospheric Imaging Assembly* (AIA: Lemen *et al.*, 2012) onboard the *Solar Dynamic Observatory* (SDO: Pesnell, Thompson, and Chamberlin, 2012). AIA's spatiotemporal resolution, sensitivity, and temperature coverage are superior to that of the *Soft X-ray Telescope* (SXT) onboard *Yohkoh*, providing the best diagnostics of the thermal plasma so far. Hence, the temperature structure of these flares is worth investigating using the new instrument. The *Reuven Ramaty High Energy Solar Spectroscopic Imager* (RHESSI: Lin *et al.*, 2002) monitors the hard X-ray (HXR) emission of flares, which is produced by bremsstrahlung radiation of both thermal and nonthermal particles. By combining observations from these two instruments, we can gain new insights into plasma heating and particle acceleration related to the magnetic reconnection processes during flares. In the sections that follow, we briefly introduce the differential emission measure (DEM) method (Section 2), analyze six candle-flame-shaped flares with this method (Section 3), and summarize the results (Section 4).

2. Instrumentation and Data Reduction

AIA onboard SDO provides full-disk images of the Sun in ten passbands almost simultaneously, with a spatial resolution of 1.5 arcseconds and a temporal cadence of 12 seconds. In this work, we use the six EUV passbands, *i.e.*, 131 Å (peak response temperature $\log T = 7.0$), 94 Å ($\log T = 6.8$), 335 Å ($\log T = 6.4$), 211 Å ($\log T = 6.3$), 193 Å ($\log T = 6.1$) and 171 Å ($\log T = 5.8$). AIA level 1 data are further processed to level 1.6 by applying the Solar Software (SSW) procedures, `aia_deconvolve_richardsonlucy` and `aia_prep`, before being used to calculate the DEM, $\varphi(T)$, which characterizes the amount of optically thin plasma at a specific temperature. In units of $\text{cm}^{-5} \text{K}^{-1}$, $\varphi(T)$ is generally given by

$$\varphi(T) = n_e^2 \left(\frac{dT}{dh} \right)^{-1}, \quad (1)$$

where $n_e(h(T))$ is the electron density at the position coordinate h along the line of sight and with temperature T . The signal g_i as detected in a specific passband i can be interpreted as

$$g_i = \int K_i(T) \varphi(T) dT + \delta g_i, \quad (2)$$

where $K_i(T)$ is the temperature response function of the passband i , and δg_i is the measurement error.

In this work, we use the code developed by Hannah and Kontar (2012) to recover the DEM. This code uses an enhanced regularization algorithm, and is capable of providing both vertical and horizontal error bars, *i.e.*, the DEM uncertainty and temperature resolution. By introducing AIA images from the six EUV channels into the code, DEM solutions can be obtained for each individual pixel in the logarithmic temperature range [5.5, 7.5], which are divided into 12 nonuniform bins as defined by the following 13 temperatures: 0.5, 1, 1.5,

2, 3, 4, 6, 8, 11, 14, 19, 25, and 32 MK, in our study. Furthermore, a DEM-weighted mean temperature $\langle T \rangle$ is defined as follows (Cheng *et al.*, 2012):

$$\langle T \rangle = \frac{\sum \varphi(T) \times T \Delta T}{\sum \varphi(T) \Delta T}, \quad (3)$$

based on which a temperature map is derived by summing over the temperature bins, with T being assigned the medium value in each bin. The uncertainty of this mean temperature is calculated by the rules for error propagation.

3. DEM Analyses of the Flares

In a survey of major flares (X-ray class M and above) observed with AIA, we selected six events exhibiting the typical cusp-shaped structure for further investigation. These flares were located close to the limb, with the axis of the flare arcade more or less aligned along the line of sight, so that the flare loop system was observed in a face-on perspective. Table 1 shows the information of these events, including the start, peak, and end time of each flare according to the GOES flare catalog (except for Flare N⁰ 2, which is missing in the GOES catalog due to a data gap of one hour before the flare, for which these data were manually determined based on the GOES X-ray lightcurve, following the same rule as GOES), the flare location, the NOAA active region from which the flare originated, and the flare category. Here the events of interest are roughly categorized as standard or non-standard flares, depending on whether they were similar to the prototypical Tsuneta flare (Tsuneta, 1996). All except Flare N⁰ 6 are long-duration events, resulting in CMEs (see the *Solar and Heliospheric Observatory/Large Angle Spectroscopic Coronagraph* CME catalog).¹ We note that GOES flare end times are defined as the time when the flux reaches half of the peak, but usually the candle-flame shape was visible far beyond the GOES end time, and it was quite steady after the flare peak despite the growth in size, as noted before (*e.g.*, Tsuneta, 1996). AIA images of major flares are often plagued by CCD saturation and diffraction patterns during the impulsive and main phases. Hence, we calculated a DEM snapshot of each candle-flame-shaped flare studied during its decay phase, with the method described in Section 2.

3.1. Standard Flares

3.1.1. Flare on 15 May 2013

The X1.2 flare on 15 May 2013 (N⁰ 1) occurred near the solar East limb in the NOAA AR 11748, associated with a fast CME (Liu, Wang, and Shen, 2014). Figure 1 shows the post-

Table 1 List of investigated flares.

N ⁰	Date	Start [UT]	Peak [UT]	End [UT]	GOES	Location	NOAA AR	Category
1	15/05/2013	01:25	01:48	01:58	X1.2	N12E64	11748	standard
2	25/09/2011	06:52	07:04	07:39	M1.3	S28W71	11303	standard
3	25/09/2011	09:25	09:35	09:53	M1.5	S28W71	11303	standard
4	25/02/2014	00:39	00:49	01:03	X4.9	S12E82	11990	standard
5	19/07/2012	04:17	05:58	06:55	M7.7	S13W88	11520	non-standard
6	27/01/2014	22:05	22:10	22:15	M4.9	S14E88	11967	non-standard

¹http://cdaw.gsfc.nasa.gov/CME_list/.

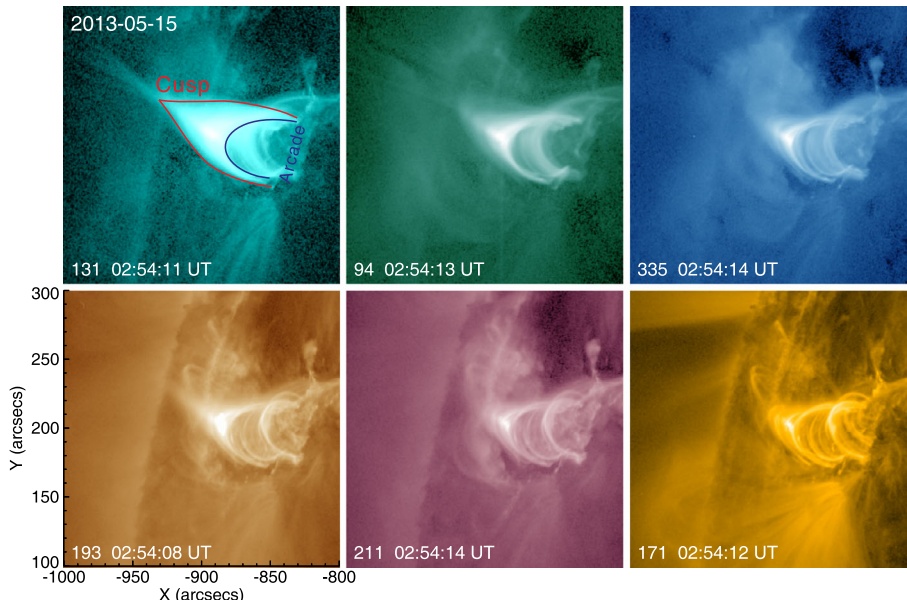


Figure 1 Candle-flame-shaped flare (N^0 1 in Table 1) on 15 May 2013 as observed in the six EUV passbands of SDO/AIA. The cusp-shaped structure and the flare arcade are illustrated by the red and blue curves, respectively.

flare arcade observed at 02:54 UT in the six EUV channels of SDO/AIA. The cusp-shaped structure can be clearly seen in 131 Å, but not in the cool passbands such as 171 Å. Thus, one can generally conclude that the cusp-shaped structure has a relatively high temperature.

The corresponding DEM maps for the 12 temperature bins are shown in Figure 2. We only show the DEM solutions whose relative uncertainties $\Delta\varphi(T)/\varphi(T) \leq 30\%$ and temperature resolution $\Delta \log T \leq 0.5$. (All the DEM maps in this article follow this criteria). We also ignore negative solutions that are sometimes returned by the regularization code. One can see that the temperature of the active-region loops is mainly below 2 MK, and that the rounded flare arcade is visible at medium temperatures, but not in high temperatures above 14 MK. In contrast, the cusp-shaped structure only appears in maps whose temperature exceeds 8 MK and can be clearly seen in temperature ranges as high as 19–25 MK. In the derived temperature map (left panel of Figure 3), the cusp-shaped structure is characterized by two high-temperature ridges, consistent with Tsuneta (1996). The map is superimposed with an HXR coronal source at 12–25 keV. The HXR image was reconstructed with the CLEAN algorithm (Hurford *et al.*, 2002), integrating over a four-minute interval around the time the AIA images were taken. Typically, the coronal source is sandwiched by the two high-temperature ridges, well beneath the tip of the cusp and slightly above the top of the flare arcade. Liu, Wang, and Shen (2014) found the HXR emission during the impulsive phase typical of a “standard” flare: the thermal component of the HXR spectrum appeared itself as a loop-top source and the nonthermal component as a pair of conjugate footpoint sources.

We selected several small box regions (indicated in the left panel of Figure 3) to plot the average DEM solutions (right panel of Figure 3). Each box includes 3 by 3 pixels. The vertical and horizontal error bars indicate the recalculated DEM and temperature uncertainties following the summation rule for error propagation. Box 1 is placed on the neighboring

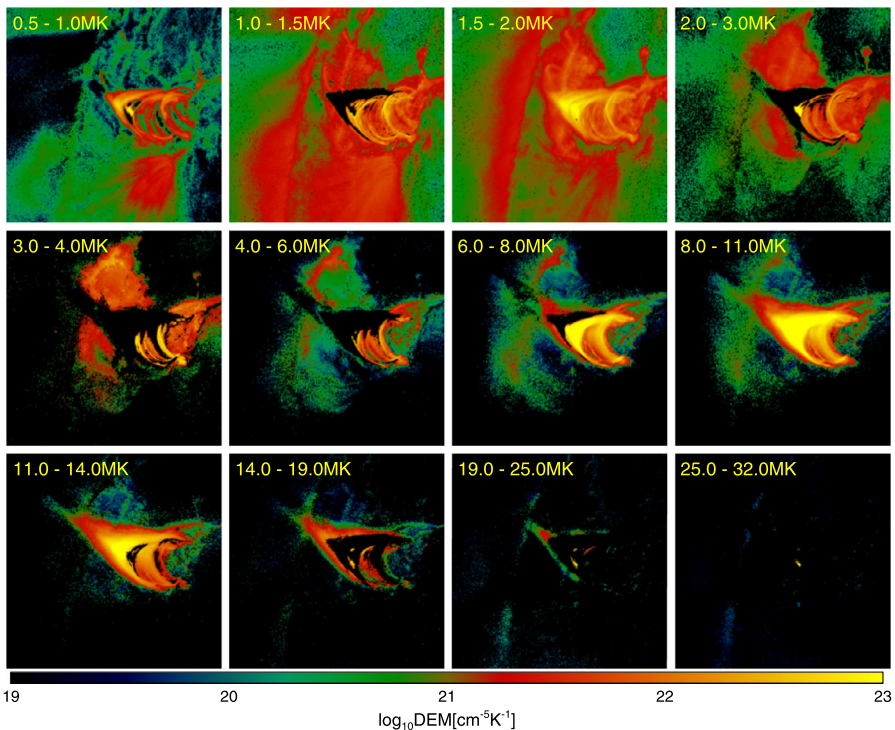


Figure 2 DEM maps in the 12 temperature bins for Flare N⁰ 1. The DEM is shown in logarithmic scale in units of $\text{cm}^{-5} \text{K}^{-1}$.

coronal loops as a reference. Boxes 2 and 4 are placed on the high-temperature ridges and Box 3 near the centroid of the HXR loop-top source. The DEM profile of coronal loops concentrates below $\log T \approx 6.3$, while that of the high-temperature ridges is characterized by a double peak, with one peak at $\log T \approx 6.2$ (“cold component” hereafter) and the other at $\log T \approx 7.0$ (“hot component” hereafter). In Box 3 we only have positive solutions in four temperature bins, but the existence of the hot component is clear. The double-peak DEM profile seems to be common for flaring plasmas (*e.g.*, Krucker and Battaglia, 2014). For each box we calculated both the mean temperature weighted by the whole DEM profile (right panel of Figure 3; denoted as $\langle T \rangle_w$ hereafter) and a “corrected” mean temperature for the double-peak DEM profile (denoted as $\langle T \rangle_h$ hereafter), which is weighted by only the hot DEM component above 4 MK ($\log T \approx 6.6$). We note that the temperature map indicates the former temperature, *i.e.*, $\langle T \rangle_w$. The agreement between the two temperatures for Boxes 2–4 is due to the dominance of the hot component over the cold component. We naturally attribute the cold component mainly to the coronal background and the hot component mainly to the flaring plasma.

3.1.2. Homologous Flares on 25 September 2011

Flares N⁰ 2 and N⁰ 3 are two homologous flares originating from the same active region, AR 11303. Both occurred on the southwestern limb on 25 September 2011, separated in time by about two hours.

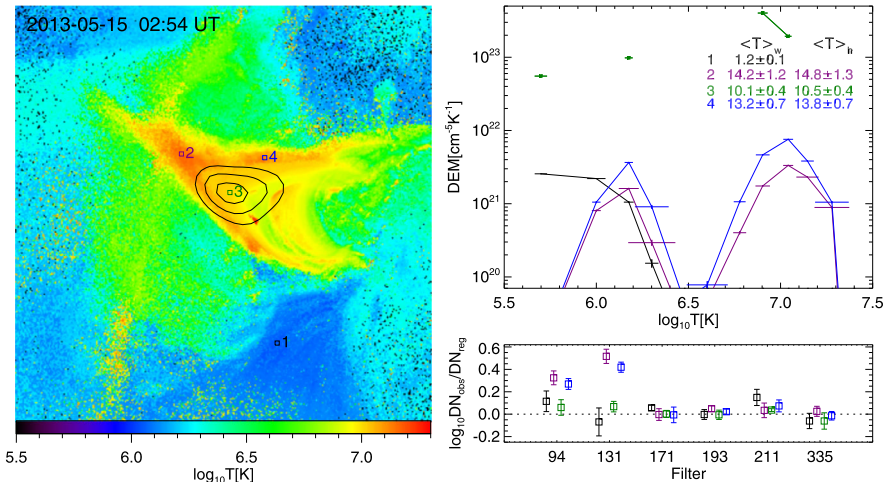


Figure 3 Temperature distribution of the flare loop system shown in Figure 1. The left panel displays the temperature map with the color scale representing $\log T$. Overplotted are contours of the HXR source at 12–25 keV reconstructed with the CLEAN algorithm. The contour levels are 50, 70, and 90 % of the maximum. The top right panel shows the DEM profile for selected regions as indicated in the left panel. Each box has a size of 3 by 3 pixels. The insets indicate the DEM-weighted mean temperature in units of MK for each box. $\langle T \rangle_w$ is weighted by the whole DEM profile, as shown in the temperature map, and $\langle T \rangle_h$ by the hot DEM component above 4 MK only. The bottom right panel plots $\log(DN_{\text{obs}}/DN_{\text{reg}})$ in function of the AIA filter, indicating how well the regularized DEM (DN_{reg}) predicts the observed flux DN_{obs} for each box in each waveband. Data points are slightly displaced for better visualization. Residual maps for each flare are available as supplementary material.

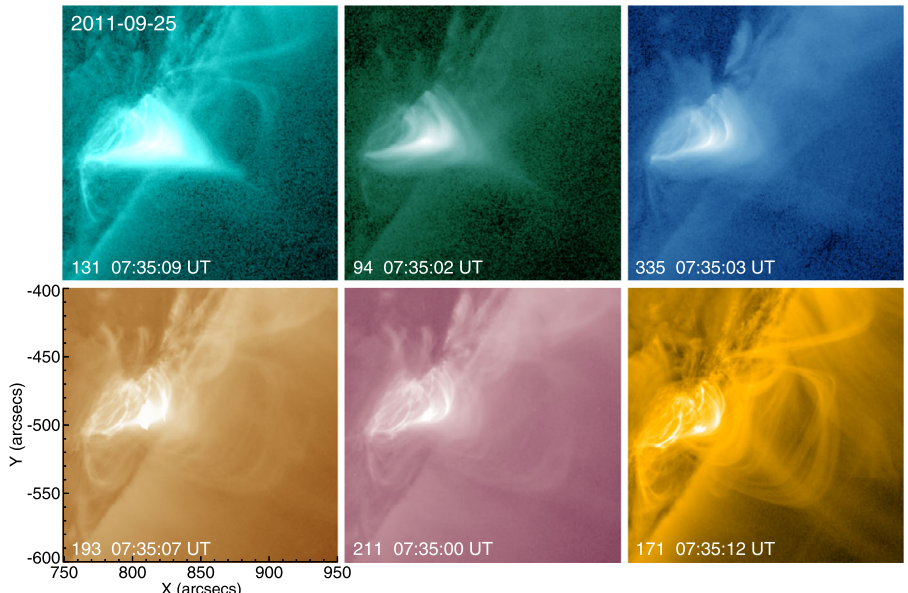


Figure 4 Candle-flame-shaped flare (N^0 2) on 25 September 2011 as observed in the six EUV passbands of SDO/AIA.

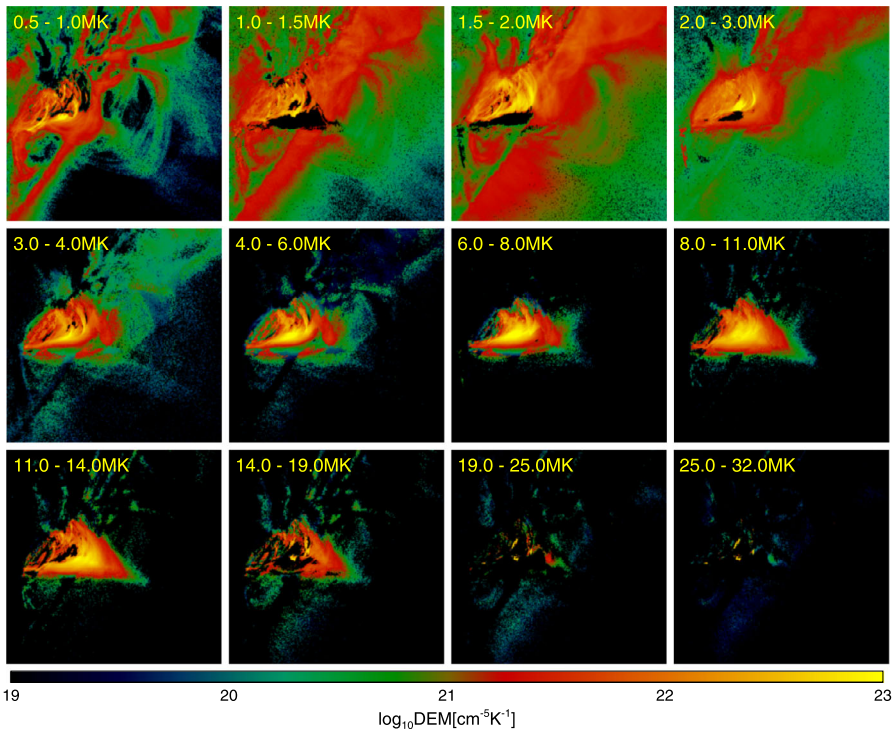


Figure 5 DEM maps in the 12 temperature bins for Flare N⁰ 2.

In Flare N⁰ 2, the cusp-shaped structure is obvious in AIA 131 Å (Figure 4) or in the DEM maps (Figure 5, 11–14 MK), but in the temperature map (left panel of Figure 6) it is not clear that there exist two high-temperature ridges: the whole cusp region appears to have similar $\langle T \rangle_w$ temperatures. By calculating $\langle T \rangle_h$, the mean temperature weighted only by the hot DEM component, one can see that the flaring plasma has cooler temperatures from the tip of the cusp (Box 2) toward the top of the flare arcade (Box 4) and that the cusp-shaped structure (Boxes 2 and 5) has higher temperatures than the flare arcade underneath. It is remarkable that the DEM profile at the top of the flare arcade (Box 4) probably shows a third peak at $\log T \approx 5.7$, which could be a signature of cooling condensation ongoing in the flare arcade.

In Flare N⁰ 3 (Figures 7, 8, and 9), we can again see the two high-temperature ridges in the temperature map (left panel of Figure 9), which is confirmed by examining the DEM profiles for selected box regions (right panel of Figure 9). We note that the remnant of the candle-flame shape from the previous flare (Flare N⁰ 2) is still visible, e.g., in AIA 131 and 94 Å (Figure 7) as well as in the DEM map at 8–11 MK (Figure 8). This may have some effect on the temperature distribution of the current flare.

3.1.3. Flare on 25 February 2014

The initiation of the X4.9 flare on 25 February 2014 (N⁰ 4) was studied in detail by Chen et al. (2014). The flare produced a typical cusp-shaped structure during the decay phase in AIA images (Figure 10). However, the flare arcade was not exactly oriented along the line

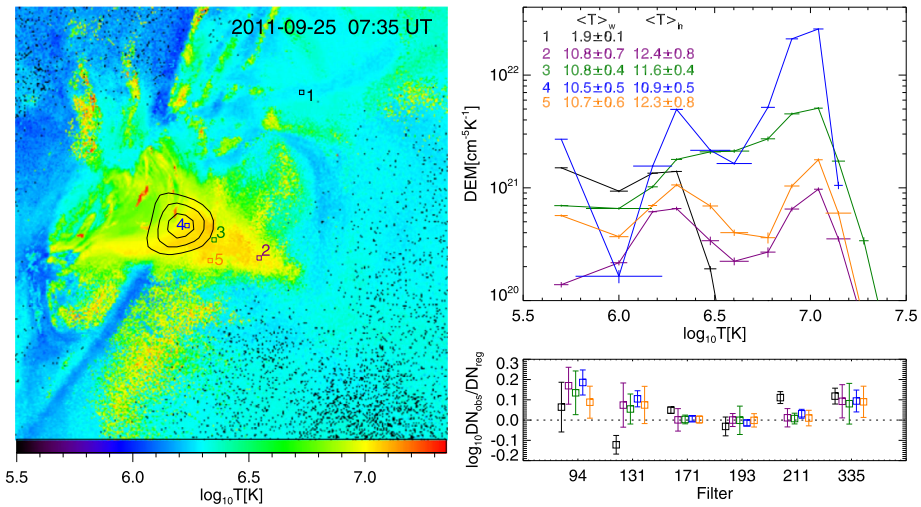


Figure 6 Temperature distribution of the flare loop system shown in Figure 4. The left panel displays the temperature map with the color scale representing $\log T$. Overplotted are contours of the HXR source at 12–25 keV reconstructed with the CLEAN algorithm. The contour levels are 50, 70, and 90 % of the maximum. The top right panel shows the DEM profile for selected regions as indicated in the left panel. Each box has a size of 3 by 3 pixels. The insets indicate the DEM-weighted mean temperature in units of MK for each box. $\langle T \rangle_w$ is weighted by the whole DEM profile, as shown in the temperature map, and $\langle T \rangle_h$ by the hot DEM component above 4 MK only. The bottom right panel plots $\log(DN_{\text{obs}}/DN_{\text{reg}})$ as a function of the AIA filter, indicating how well the regularized DEM (DN_{reg}) predicts the observed flux DN_{obs} for each box in each waveband. Data points are slightly displaced for better visualization. Residual maps for the flare are available as supplementary material.

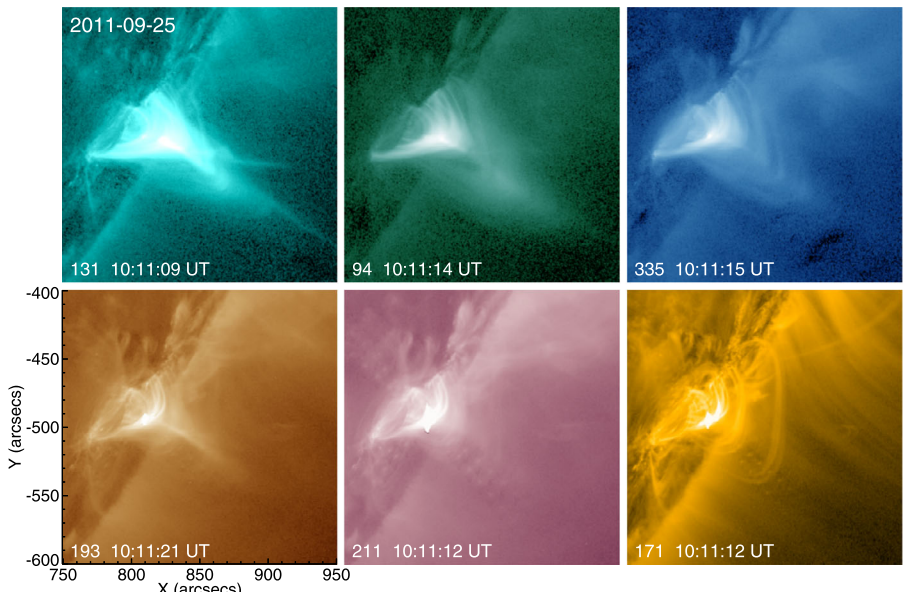


Figure 7 Candle-flame-shaped flare (N^0 3) on 25 September 2011 as observed in the six EUV passbands of SDO/AIA.

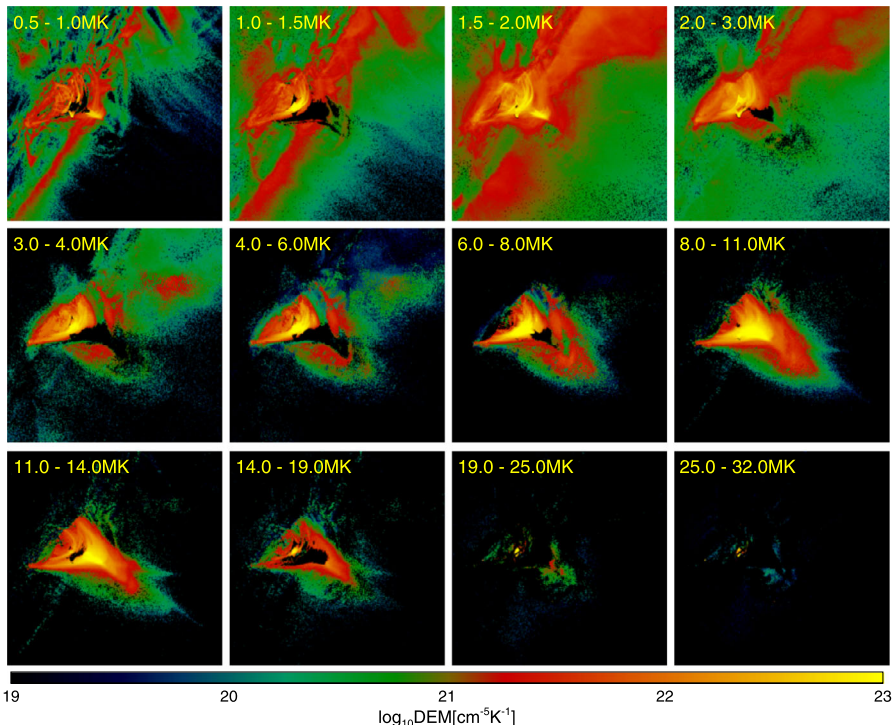


Figure 8 DEM maps in the 12 temperature bins for Flare N° 3.

of sight, but in a southeast – northwest direction, so that it was observed with AIA in an oblique perspective, presumably due to which emission from the cusp-shaped structure was relatively weak, resulting in larger uncertainties in the DEM calculation. In spite of that, the overall temperature distribution is consistent with the standard picture. As can be seen from the DEM maps (Figure 11), the cusp-shaped structure is visible in high temperatures (11–19 MK), while the rounded flare arcade is detected below 14 MK.

In the temperature map that displays $\langle T \rangle_w$ for each pixel (left panel of Figure 12), however, the cusp structure appears to have a similar mean temperature as the rounded flare arcade underneath. This is due to the existence of a relatively strong coronal background, which shows up in the AIA cool passbands, 193, 211, and 171 Å, as diffuse emission and coronal loops behind the flare loop system of interest. The 131 and 94 Å passbands also show some hot diffuse emission in the shape of an arcade of loops oriented in the north-south direction, which appears to be the remnants from preceding limb flares, most likely the M1.2 flare (S11E88) peaking at 11:17 UT on 24 February 2014. The RHESSI quick-look image at 6–12 keV did show an elongated source in a similar direction.² Examining the DEM profile for selected regions, one can see that the cool component dominates the hot component for Boxes 2 and 4, which are placed at the edge of the cusp (right panel of Figure 12). With the strong coronal background, $\langle T \rangle_h$ is a more appropriate representation of the flaring plasma temperature than $\langle T \rangle_w$. Indeed, the standard temperature distribution is recovered with $\langle T \rangle_h$.

²<http://sprg.ssl.berkeley.edu/~tohban/browser/>.

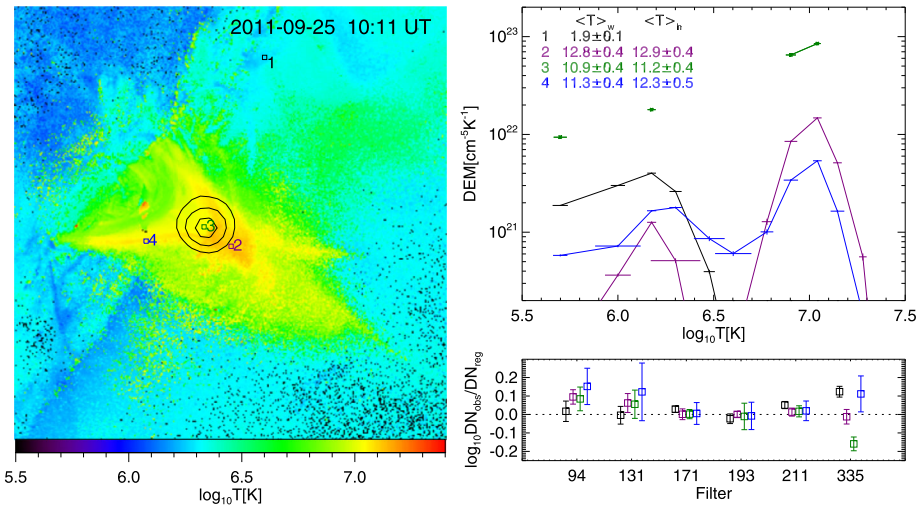


Figure 9 Temperature distribution of the flare loop system shown in Figure 7. The left panel displays the temperature map with the color scale representing $\log T$. Overplotted are contours of the HXR source at 12–25 keV reconstructed with the CLEAN algorithm. The contour levels are 50, 70, and 90 % of the maximum. The top right panel shows the DEM profile for selected regions as indicated in the left panel. Each box has a size of 3 by 3 pixels. The insets indicate the DEM-weighted mean temperature in units of MK for each box. $\langle T \rangle_w$ is weighted by the whole DEM profile, as shown in the temperature map, and $\langle T \rangle_h$ by the hot DEM component above 4 MK only. The bottom right panel plots $\log(\text{DN}_{\text{obs}}/\text{DN}_{\text{reg}})$ as a function of the AIA filter, indicating how well the regularized DEM (DN_{reg}) predicts the observed flux DN_{obs} for each box in each waveband. Data points are slightly displaced for better visualization. Residual maps for each flare are available as supplementary material.

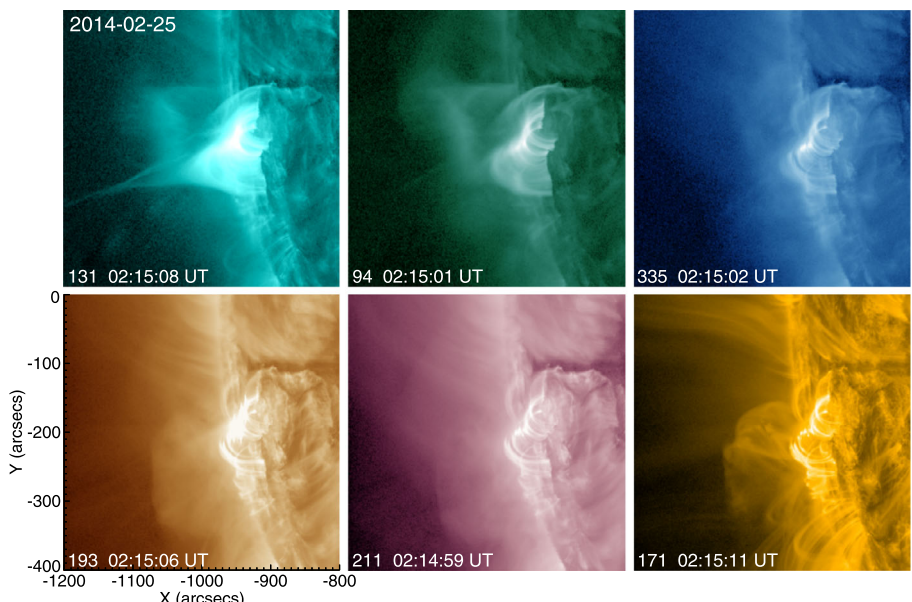


Figure 10 Candle-flame-shaped flare ($N^0 4$) on 25 February 2014 as observed in the six EUV passbands of SDO/AIA.

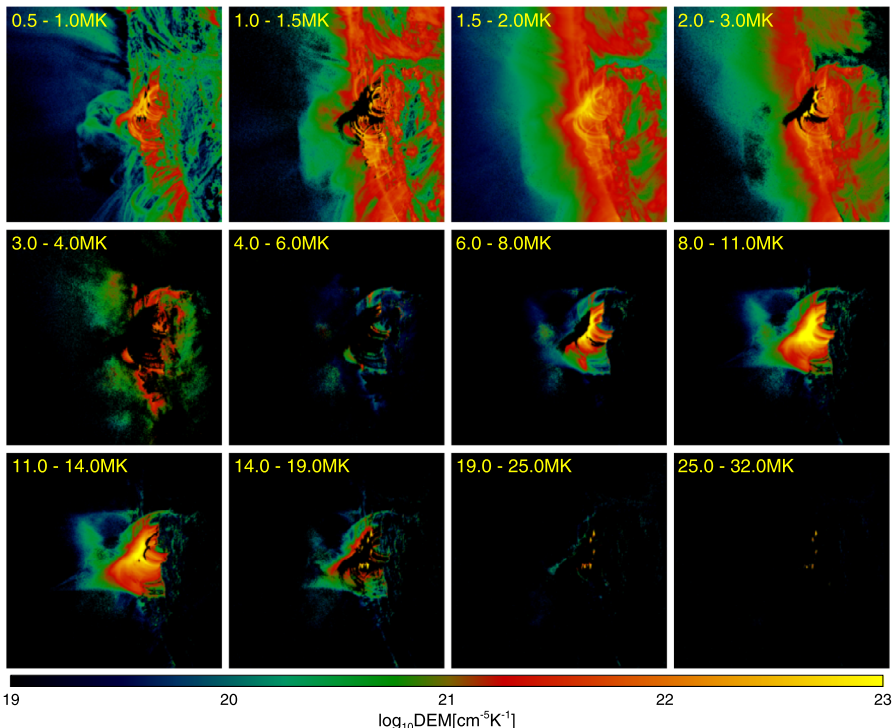


Figure 11 DEM maps in the 12 temperature bins for Flare N° 4.

3.2. Non-standard Flares

3.2.1. Flare on 19 July 2012

The M7.7 flare on 19 July 2012 (Flare N° 5) has been studied in detail by Liu (2013), Liu, Chen, and Petrosian (2013), Krucker and Battaglia (2014), and Sun, Cheng, and Ding (2014). The most intriguing features of this flare include a nonthermal above-the-loop-top HXR source at 30–80 keV during the impulsive phase (Liu, Chen, and Petrosian, 2013; Krucker and Battaglia, 2014), which is very similar to the famous “Masuda flare” (Masuda et al., 1994; Liu, Xu, and Wang, 2011), and the fast retraction of cusp-shaped flare loops at speeds of hundreds of kilometers *per* second mainly during the decay phase (Liu, Chen, and Petrosian, 2013; Liu, 2013).

Figure 13 shows the post-flare arcade observed at 06:40 UT with SDO/AIA. In the corresponding DEM maps (Figure 14), the rounded flare arcade is visible below 14 MK, while the cusp-shaped structure appears at 8–32 MK. In general, cooler loops are nested below hotter ones, consistent with the standard picture, but it is remarkable that the entire cusp region becomes prominent at 19–25 MK and that the region beneath the tip of the cusp is even more prominent than the two high-temperature ridges. In the temperature map (left panel of Figure 15), one can also see that the hottest region is above the top of the rounded flare arcade and beneath the tip of the cusp. This region is slightly above the HXR loop-top centroid. We selected several small box regions to plot the average DEM solutions. Each box includes 6 by 6 pixels (for better statistics, we use larger box sizes for larger flares). Box 1 is selected on the diffuse coronal emission outside of the cusp-shaped structure as a

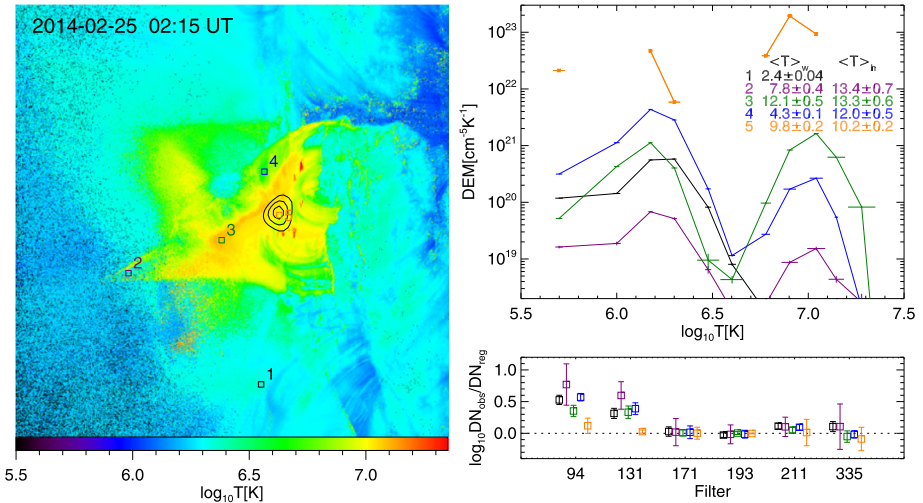


Figure 12 Temperature distribution of the flare loop system shown in Figure 10. The left panel displays the temperature map with the color scale representing $\log T$. Overplotted are contours of the HXR source reconstructed with the CLEAN algorithm. The contour levels are 50, 70, and 90 % of the maximum. The top right panel shows the DEM profile for selected regions as indicated in the left panel. Each box has a size of 6 by 6 pixels. The insets indicate the DEM-weighted mean temperature in units of MK for each box. $\langle T \rangle_w$ is weighted by the whole DEM profile, as shown in the temperature map, and $\langle T \rangle_h$ by the hot DEM component above 4 MK only. The bottom right panel plots $\log(DN_{\text{obs}}/DN_{\text{reg}})$ as a function of the AIA filter, indicating how well the regularized DEM (DN_{reg}) predicts the observed flux DN_{obs} for each box in each waveband. Data points are slightly displaced for better visualization. Residual maps for the flare are available as supplement material.

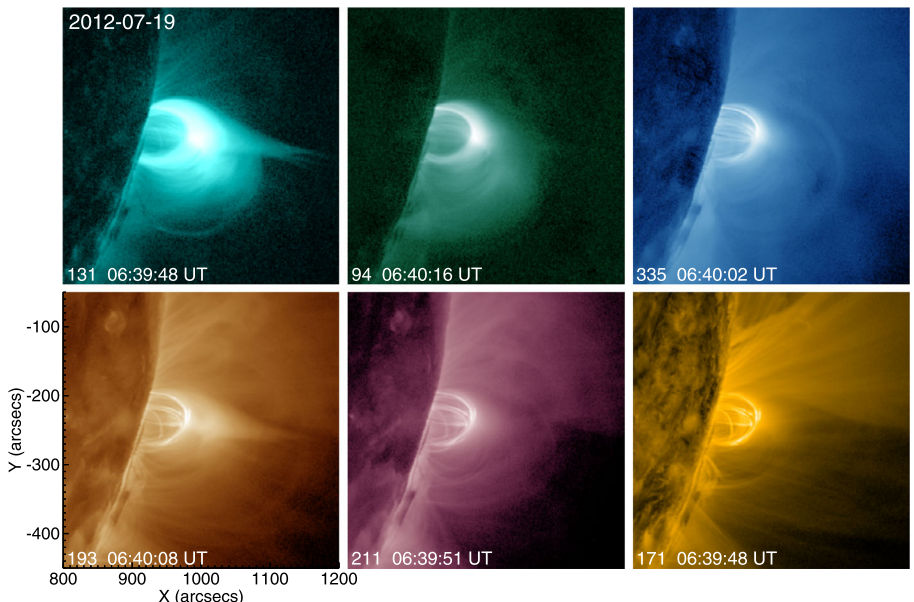


Figure 13 Candle-flame-shaped flare (N⁰ 5) on 19 July 2012 as observed by the six EUV passbands of SDO/AIA.

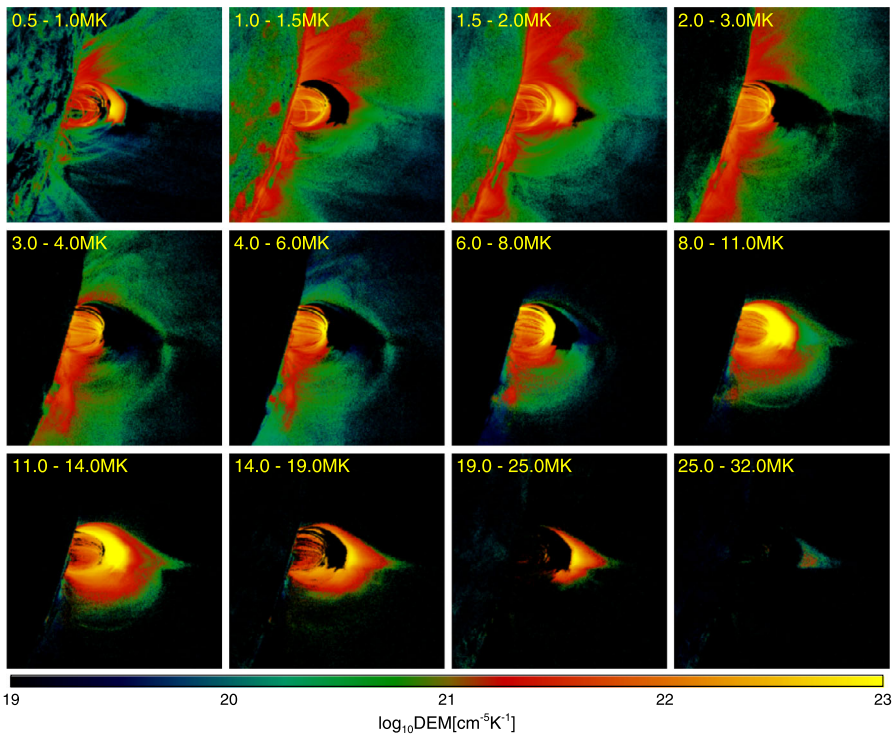


Figure 14 DEM maps in the 12 temperature bins for Flare N° 5.

reference, one can see that its DEM profile has a major peak around $\log T \approx 6.0$ as well as a negligible hot component around $\log T \approx 7.0$. In contrast, the peak of the hot component in the other box regions is as significant as or even stronger than the peak of the cold component. As a result, $\langle T \rangle_h$ is not very different from $\langle T \rangle_w$. Furthermore, the hot peak shifts toward higher temperatures for boxes at lower altitudes (Boxes 2–4). This results in an increase in the mean temperature from the tip of the cusp toward the HXR loop-top source. On the other hand, the cusp-shaped structure still has similar temperatures (Boxes 2 and 5). This distribution is very different from the prototypical temperature structure in the Tsuneta flare (Tsuneta, 1996), and hence excludes the reconnection site or the slow-mode shocks attached to it as the primary energy source for the heated plasma enclosed by the cusp-shaped structure.

Our analysis largely confirms the result by Liu, Chen, and Petrosian (2013), who employed a forward-fitting DEM algorithm assuming a Gaussian DEM profile and noted that the high-temperature region is close to the HXR loop-top centroid during the decay phase. Combining HXR and EUV observations, Liu, Chen, and Petrosian (2013) attributed both primary plasma heating and particle acceleration to the reconnection outflows, in which fast-mode shocks and turbulence may be at work. Krucker and Battaglia (2014) proposed that the above-the-loop-top source is the acceleration region where all the electrons are accelerated through a bulk energization process. They also noted, however, that there exists no EUV source corresponding to the HXR above-the-loop-top source during the impulsive phase when this nonthermal HXR source is visible. Hence, there are two possibilities, either that plasma heating and particle acceleration are due to different mechanisms, or that the

same mechanism accelerates particles during the impulsive phase while it heats the plasma during the decay phase, as reconnection proceeds to greater altitudes.

3.2.2. Flare on 2014 January 27

The M4.9 flare on 27 January 2014 (Flare N⁰ 6) occurred on the southeastern limb. It was preceded by several homologous flares in the same active region and resulted in no CME. Apparently involving a multipolar magnetic field, the flare loop system exhibited a double candle-flame configuration in the AIA hot passbands, 131 and 94 Å (Figure 16), and also in the corresponding DEM maps at about 8–14 MK (Figure 17). The two candle flames are located side by side (Figure 16), sharing a much larger cusp-shaped structure, whose sharp edges are suggestive of magnetic separatrices. Both the morphology and temperature distribution (see below) are similar to the flare studied by Guidoni *et al.* (2015), except for the appreciable asymmetry between the two candle flames in their case (see, for example, their Figure 6). The 12–25 keV RHESSI contours superimposed on the temperature map (Figure 18) were characterized by three sources. Each candle flame is apparently associated with an X-ray source, and a third source is located at higher altitude, beneath the tip of the shared cusp.

The temperature distribution of this flare seems quite different from the confined flare investigated by Liu *et al.* (2014). Despite being categorized as a non-standard flare mainly because of the multipolar configuration, the cusp-shaped structure in the studied flare was still hotter than the flare arcade underneath (Figure 18), which agrees in this aspect with the Tsuneta flare. In contrast, the temperature distribution in Liu *et al.* (2014) is similar to that in Flare N⁰ 5 (see Section 3.2.1), with a hot flare arcade and a cooler cusp. We note that Liu *et al.* (2014) employed a different DEM method by fitting the DEM profile with spline functions (Cheng *et al.*, 2012) and calculated $\langle T \rangle_w$ instead of $\langle T \rangle_h$. Applying the current DEM method to the same flare studied by Liu *et al.* (2014), we obtain with $\langle T \rangle_h$ a similar result as Liu *et al.* (2014). The similarity is due to the dominance of the hot component. However, the flare arcade in Liu *et al.* (2014) was observed in a side-on view, whereas the flare studied here is in a face-on view, it is hence unclear whether the projection effect has an impact on the DEM result. In addition, it is difficult to find out the exact magnetic configuration of this flare because it occurred on the limb, whereas the flare in Liu *et al.* (2014) clearly involved a tripolar configuration. The detailed magnetic topology should play a critical role in the resultant temperature distribution.

3.3. Emission Measure

Integrating the DEM over temperatures above 4 MK, we constructed an emission measure (EM; cm⁻⁵) of the flaring plasmas by leaving out the cold component. The resultant EM maps (Figure 19) mimic what one should see with a broadband soft X-ray imager like *Yohkoh*/SXT and the *X-ray Telescope* (XRT) onboard *Hinode*, featuring both the cusp-shaped structure (Tsuneta *et al.*, 1992; Tsuneta, 1996) and the intensity enhancement at the top of the flare arcade (Tsuneta *et al.*, 1992; McTiernan *et al.*, 1993; Feldman *et al.*, 1994). In particular, the thermal HXR loop-top source is observed to be co-spatial with this EM-enhanced region.

However, for both standard and non-standard flares, a particular feature discovered in the Tsuneta flare (Tsuneta, 1996) is missing (see also Guidoni *et al.*, 2015), which is a relatively cool (6–8 MK) and dense channel extending from the cusp region all the way down to the innermost visible arch of the flare arcade, also called a trunk-like feature (Forbes and Acton, 1996). Tsuneta (1996) identified this trunk-like feature as the cooled reconnection

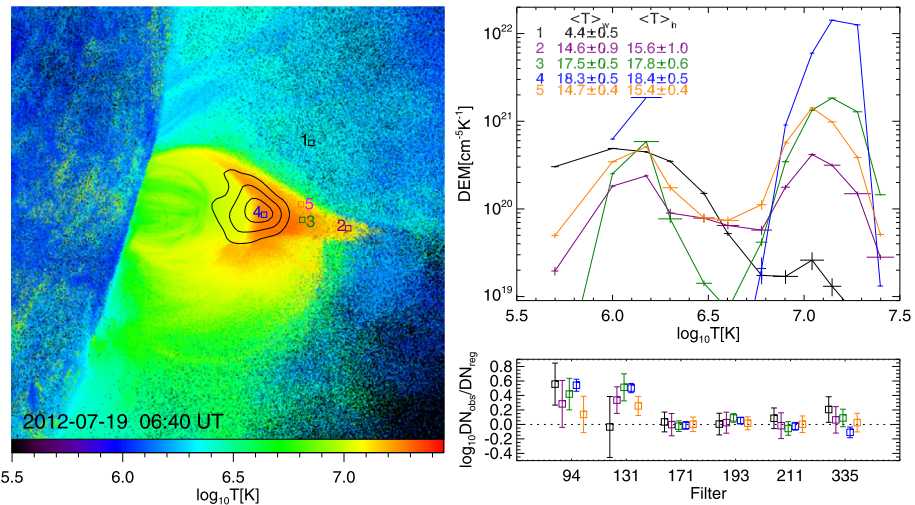


Figure 15 Temperature distribution of the flare loop system shown in Figure 13. The left panel displays the temperature map with the color scale representing $\log T$. Overplotted are contours of the HXR source reconstructed with the CLEAN algorithm. The contour levels are 50, 70, and 90 % of the maximum. The top right panel shows the DEM profile for selected regions as indicated in the left panel. Each box has a size of 6 by 6 pixels. The insets indicate the DEM-weighted mean temperature in units of MK for each box. $\langle T \rangle_w$ is weighted by the whole DEM profile, as shown in the temperature map, and $\langle T \rangle_h$ by the hot DEM component above 4 MK only. The bottom right panel plots $\log(\text{DN}_{\text{obs}} / \text{DN}_{\text{reg}})$ as a function of the AIA filter, indicating how well the regularized DEM (DN_{reg}) predicts the observed flux DN_{obs} for each box in each waveband. Data points are slightly displaced for better visualization. Residual maps for the flare are available as supplementary material.

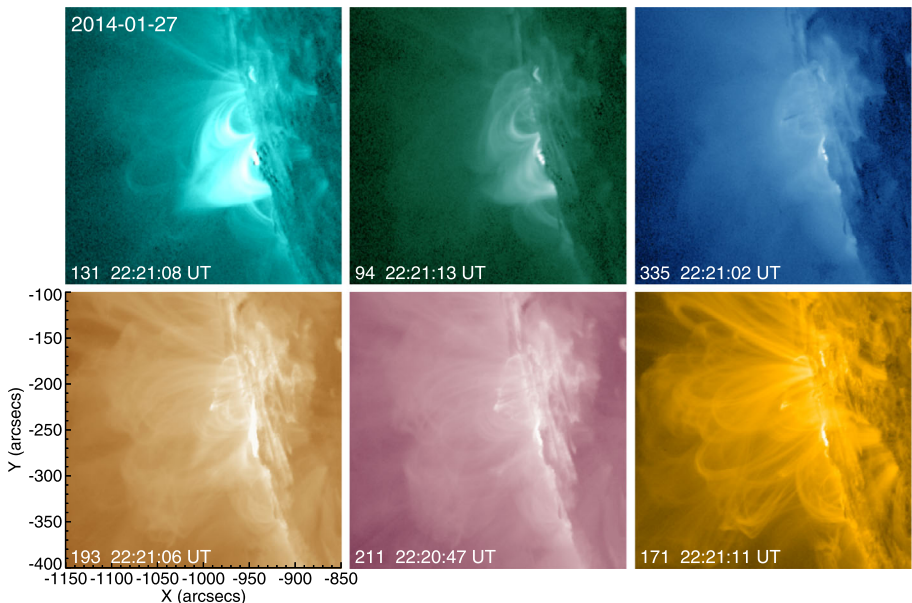


Figure 16 Flare with a double candle-flame configuration (N⁰ 6 in Table 1) observed with the six EUV passbands of SDO/AIA on 27 January 2014.

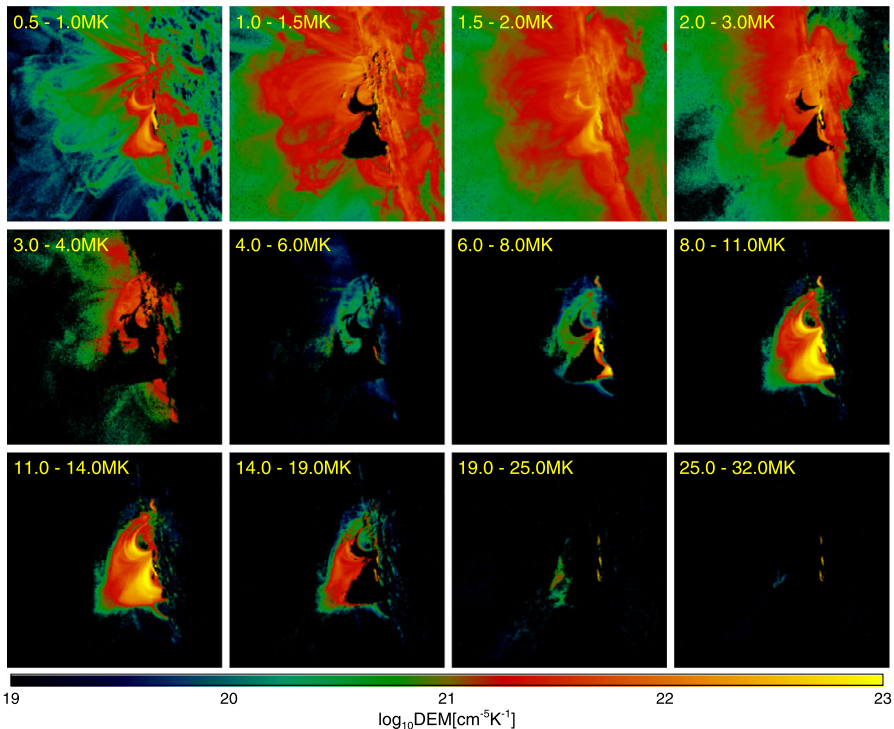


Figure 17 DEM maps in the temperature bins for Flare N^0 6.

outflow and explained its absence by the short distance between the reconnection site and the flare arcade, *i.e.*, the outflow reaches the arcade too soon to cool down. Forbes and Acton (1996) suggested that the lower part of the trunk-like feature is not a reconnection jet, but a region of enhanced cooling, where a radiative thermal instability is triggered by the reconnection outflow. They also argued that it is absence of a cool and dense channel because the downward reconnection jet is also absent in weak events. Our study appears to contradict both interpretations, because in Flares N^0 1 and 5, the tip of the cusp, *i.e.*, the alleged reconnection site, is sufficiently far away from the flare arcade, compared with the Tsuneta flare, and both are even more energetic than the Tsuneta flare (which was an M3.2).

4. Conclusions

The DEM analysis on candle-flame-shaped flares reveals that the DEM profile of the flaring plasma generally has a double-peak distribution in temperature, with a cold component around $\log T \approx 6.2$ and a hot component around $\log T \approx 7.0$. The former is mainly attributed to emission not related to the flare, *i.e.*, from the foreground and background coronal plasma (generally termed “coronal background”). Hence, the mean temperature weighted by the hot DEM component, $\langle T \rangle_h$, is a better representation of the flaring plasma than the conventionally defined mean temperature, $\langle T \rangle_w$, which is weighted by the whole DEM profile including the cold component. With the presence of a strong coronal background, the latter could significantly underestimate the temperature of the flaring plasma, as in the case of

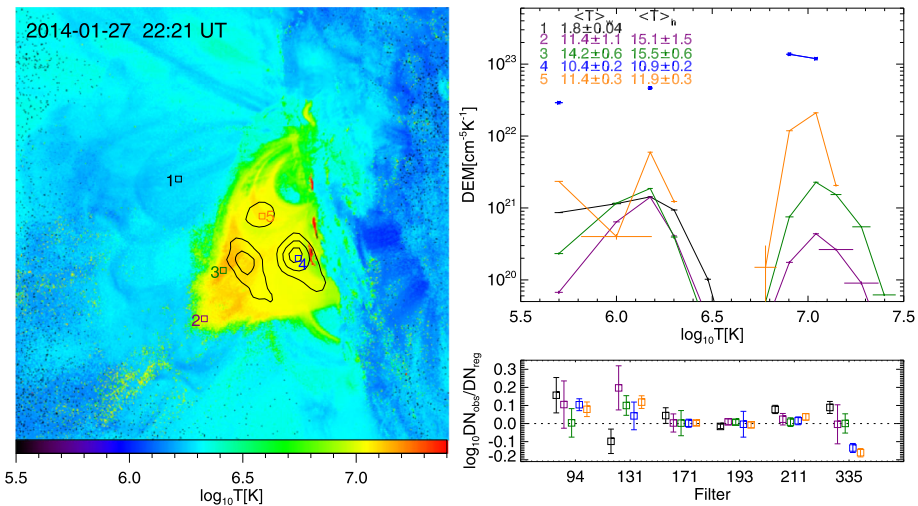


Figure 18 Temperature distribution of the flare loop system shown in Figure 16. The left panel displays the temperature map with the color scale representing $\log T$. Overplotted are contours of the HXR source reconstructed with the CLEAN algorithm. The contour levels are 50, 70, and 90 % of the maximum. The top right panel shows the DEM profile for selected regions as indicated in the left panel. Each box has a size of 5 by 5 pixels. The insets indicate the DEM-weighted mean temperature in units of MK for each box. $\langle T \rangle_w$ is weighted by the whole DEM profile, as shown in the temperature map, and $\langle T \rangle_h$ by the hot DEM component above 4 MK only. The bottom right panel plots $\log(DN_{\text{obs}}/DN_{\text{reg}})$ as a function of the AIA filter, indicating how well the regularized DEM (DN_{reg}) predicts the observed flux DN_{obs} for each box in each waveband. Data points are slightly displaced for better visualization. Residual maps for the flare are available as supplementary material.

Flare N⁰ 4. The fact that the cusp-shaped structure has roughly the same $\langle T \rangle_h$ (Figures 3, 6, 9, 12, 15, and 18) corroborates the appropriateness of this approach, because the thermal conduction is assumed to be highly efficient along the newly reconnected field lines that outline the cusp-shaped structure. Along the same train of thought, we propose that the EM integrating over high temperatures is also a better representation of the flaring plasma. The absence of a cool and dense channel, or trunk-like feature, in all of the investigated flares, however, poses a challenge to the previous hypothesis on the formation mechanism of such a feature. We note that the regularized DEMs tend to underestimate fluxes observed in the 94 and 131 Å passbands (Figures 3, 6, 9, 12, 15, and 18), therefore underestimating the hot DEM component as the 94 and 131 Å filters are its major contributors. This further justifies the above approach.

The majority of the candle-flame-shaped flares in our study resemble the famous Tsuneta flare in temperature distribution, *i.e.*, the cusp-shaped structure has higher temperatures than the rounded flare arcade underneath. Roughly speaking, this includes the confined flare (N⁰ 6) with a double candle-flame shape sharing the same cusp-shaped structure. Our analysis hence corroborates the classic reconnection model, in which the slow-mode shocks attached to the reconnection site play a significant role in heating the plasma.

The 19 July 2012 flare (N⁰ 5) is a very intriguing exception: the temperature decreases with altitude from the tip of the cusp toward the top of the arcade. The hottest region is slightly above the X-ray loop-top source that is normally co-spatial with the EM-enhanced region at the top of the arcade. It is not clear whether this abnormal temperature distribution is related to the rare above-the-loop-top source observed during the impulsive phase, but it

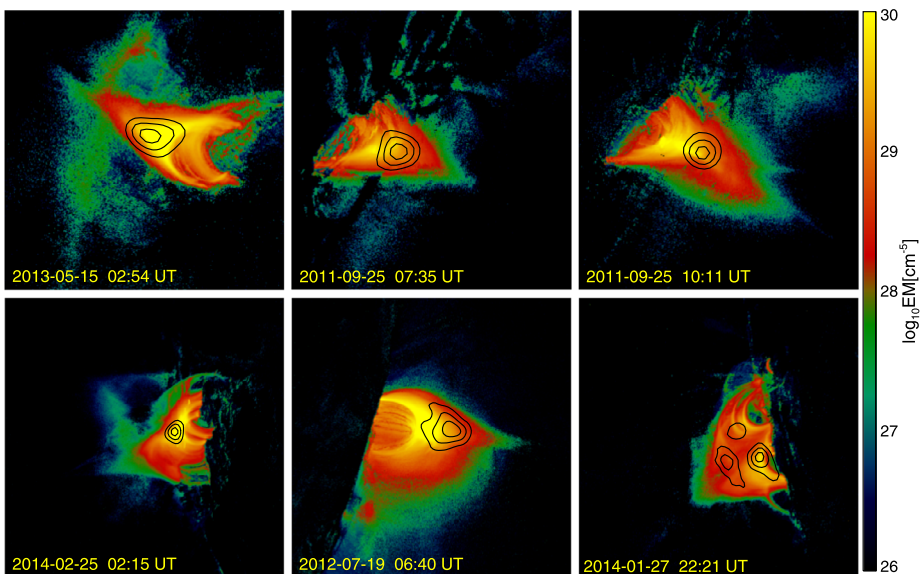


Figure 19 Emission measure of the hot plasma above 4 MK in the studied flares. Each map is superimposed by HXR sources at 12–25 keV, with contour levels at 50, 70, and 90 % of the maximum brightness in each individual RHESSI image.

means that a different heating mechanism from the slow-mode shocks is at work in the cusp region, which is most likely related to the reconnection outflow. However, it is difficult to understand why in other flares this heating mechanism appears to be insignificant. These issues are worth of further investigation.

Acknowledgements We are grateful to the SDO team for the free access to the data and the development of the data analysis software. R. Liu acknowledges the Thousand Young Talents Program of China, NSFC 41222031 and 41474151, and NSF AGS-1153226. This work was also supported by NSFC 41131065 and 41121003, 973 key project 2011CB811403, CAS Key Research Program KZZD-EW-01-4, the fundamental research funds for the central universities WK2080000031.

References

- Antiochos, S.K., Sturrock, P.A.: 1978, Evaporative cooling of flare plasma. *Astrophys. J.* **220**, 1137. DOI. [ADS](#).
- Carmichael, H.: 1964, A process for flares. *NASA Spec. Publ.* **50**, 451. [ADS](#).
- Chen, H., Zhang, J., Cheng, X., Ma, S., Yang, S., Li, T.: 2014, Direct observations of Tether-cutting reconnection during a major solar event from 2014 February 24 to 25. *Astrophys. J. Lett.* **797**, L15. DOI. [ADS](#).
- Cheng, X., Zhang, J., Saar, S.H., Ding, M.D.: 2012, Differential emission measure analysis of multiple structural components of coronal mass ejections in the inner corona. *Astrophys. J.* **761**, 62. DOI. [ADS](#).
- Feldman, U., Seely, J.F., Doschek, G.A., Strong, K.T., Acton, L.W., Uchida, Y., Tsuneta, S.: 1994, The morphology of the 10^7 K plasma in solar flares. 1: Nonimpulsive flares. *Astrophys. J.* **424**, 444. DOI. [ADS](#).
- Fletcher, L., Dennis, B.R., Hudson, H.S., Krucker, S., Phillips, K., Veronig, A., Battaglia, M., Bone, L., Caspi, A., Chen, Q., Gallagher, P., Grigis, P.T., Ji, H., Liu, W., Milligan, R.O., Temmer, M.: 2011, An observational overview of solar flares. *Space Sci. Rev.* **159**, 19. DOI. [ADS](#).
- Forbes, T.G., Acton, L.W.: 1996, Reconnection and field line shrinkage in solar flares. *Astrophys. J.* **459**, 330. DOI. [ADS](#).

- Guidoni, S.E., McKenzie, D.E., Longcope, D.W., Plowman, J.E., Yoshimura, K.: 2015, Temperature and electron density diagnostics of a candle-flame-shaped flare. *Astrophys. J.* **800**, 54. [DOI](#). [ADS](#).
- Hannah, I.G., Kontar, E.P.: 2012, Differential emission measures from the regularized inversion of Hinode and SDO data. *Astron. Astrophys.* **539**, A146. [DOI](#). [ADS](#).
- Hirayama, T.: 1974, Theoretical model of flares and prominences. I: Evaporating flare model. *Solar Phys.* **34**, 323. [DOI](#). [ADS](#).
- Hurford, G.J., Schmahl, E.J., Schwartz, R.A., Conway, A.J., Aschwanden, M.J., Csillagh, A., Dennis, B.R., Johns-Krull, C., Krucker, S., Lin, R.P., McTiernan, J., Metcalf, T.R., Sato, J., Smith, D.M.: 2002, The RHESSI imaging concept. *Solar Phys.* **210**, 61. [DOI](#). [ADS](#).
- Kopp, R.A., Pneuman, G.W.: 1976, Magnetic reconnection in the corona and the loop prominence phenomenon. *Solar Phys.* **50**, 85. [DOI](#). [ADS](#).
- Krucker, S., Battaglia, M.: 2014, Particle densities within the acceleration region of a solar flare. *Astrophys. J.* **780**, 107. [DOI](#). [ADS](#).
- Lemen, J.R., Title, A.M., Akin, D.J., Boerner, P.F., et al.: 2012, The Atmospheric Imaging Assembly (AIA) on the Solar Dynamics Observatory (SDO). *Solar Phys.* **275**, 17. [DOI](#). [ADS](#).
- Lin, R.P., Dennis, B.R., Hurford, G.J., Smith, D.M., et al.: 2002, The Reuven Ramaty High-Energy Solar Spectroscopic Imager (RHESSI). *Solar Phys.* **210**, 3. [DOI](#). [ADS](#).
- Liu, R.: 2013, Dynamical processes at the vertical current sheet behind an erupting flux rope. *Mon. Not. Roy. Astron. Soc.* **434**, 1309. [DOI](#). [ADS](#).
- Liu, R., Wang, Y., Shen, C.: 2014, Early evolution of an energetic coronal mass ejection and its relation to EUV waves. *Astrophys. J.* **797**, 37. [DOI](#). [ADS](#).
- Liu, R., Xu, Y., Wang, H.: 2011, A revisit of the Masuda flare. *Solar Phys.* **269**, 67. [DOI](#). [ADS](#).
- Liu, R., Titov, V.S., Gou, T., Wang, Y., Liu, K., Wang, H.: 2014, An unorthodox X-class long-duration confined flare. *Astrophys. J.* **790**, 8. [DOI](#). [ADS](#).
- Liu, W., Chen, Q., Petrosian, V.: 2013, Plasmoid ejections and loop contractions in an eruptive M7.7 solar flare: evidence of particle acceleration and heating in magnetic reconnection outflows. *Astrophys. J.* **767**, 168. [DOI](#). [ADS](#).
- Masuda, S., Kosugi, T., Hara, H., Tsuneta, S., Ogawara, Y.: 1994, A loop-top hard X-ray source in a compact solar flare as evidence for magnetic reconnection. *Nature* **371**, 495. [DOI](#). [ADS](#).
- McTiernan, J.M., Kane, S.R., Loran, J.M., Lemen, J.R., Acton, L.W., Hara, H., Tsuneta, S., Kosugi, T.: 1993, Temperature and density structure of the 1991 November 2 flare observed by the YOHKOH soft X-ray telescope and hard X-ray telescope. *Astrophys. J. Lett.* **416**, L91. [DOI](#). [ADS](#).
- Ogawara, Y., Takano, T., Kato, T., et al.: 1991, The solar-A mission – an overview. *Solar Phys.* **136**, 1. [DOI](#). [ADS](#).
- Pesnell, W.D., Thompson, B.J., Chamberlin, P.C.: 2012, The Solar Dynamics Observatory (SDO). *Solar Phys.* **275**, 3. [DOI](#). [ADS](#).
- Priest, E.R., Forbes, T.G.: 1986, New models for fast steady state magnetic reconnection. *J. Geophys. Res.* **91**, 5579. [DOI](#). [ADS](#).
- Priest, E.R., Forbes, T.G.: 2002, The magnetic nature of solar flares. *Astron. Astrophys. Rev.* **10**, 313. [DOI](#). [ADS](#).
- Reeves, K.K., Seaton, D.B., Forbes, T.G.: 2008, Field line shrinkage in flares observed by the X-ray telescope on Hinode. *Astrophys. J.* **675**, 868. [DOI](#). [ADS](#).
- Schmieder, B., Forbes, T.G., Malherbe, J.M., Machado, M.E.: 1987, Evidence for gentle chromospheric evaporation during the gradual phase of large solar flares. *Astrophys. J.* **317**, 956. [DOI](#). [ADS](#).
- Sheeley, N.R. Jr., Howard, R.A., Koonen, M.J., Michels, D.J.: 1983, Associations between coronal mass ejections and soft X-ray events. *Astrophys. J.* **272**, 349. [DOI](#). [ADS](#).
- Shibata, K., Magara, T.: 2011, Solar flares: magnetohydrodynamic processes. *Living Rev. Solar Phys.* **8**, 6. [DOI](#). [ADS](#).
- Sturrock, P.A.: 1966, Model of the high-energy phase of solar flares. *Nature* **211**, 695. [DOI](#). [ADS](#).
- Sun, J.Q., Cheng, X., Ding, M.D.: 2014, Differential emission measure analysis of a limb solar flare on 2012 July 19. *Astrophys. J.* **786**, 73. [DOI](#). [ADS](#).
- Titov, V.S., Hornig, G., Démoulin, P.: 2002, Theory of magnetic connectivity in the solar corona. *J. Geophys. Res.* **107**, 1164. [DOI](#). [ADS](#).
- Tsuneta, S.: 1996, Structure and dynamics of magnetic reconnection in a solar flare: Erratum. *Astrophys. J.* **464**, 1055. [DOI](#). [ADS](#).
- Tsuneta, S., Hara, H., Shimizu, T., Acton, L.W., Strong, K.T., Hudson, H.S., Ogawara, Y.: 1992, Observation of a solar flare at the limb with the YOHKOH soft X-ray telescope. *Publ. Astron. Soc. Japan* **44**, L63. [ADS](#).
- Webb, D.F., Hundhausen, A.J.: 1987, Activity associated with the solar origin of coronal mass ejections. *Solar Phys.* **108**, 383. [DOI](#). [ADS](#).